

Comparison of advanced gravitational-wave detectors

Gregory M. Harry*

Department of Physics, Syracuse University, Syracuse, New York 13244-1130

Janet L. Houser†

LIGO Visiting Scientist, Massachusetts Institute of Technology, Room NW17-161, 175 Albany Street, Cambridge, Massachusetts, 02139

Kenneth A. Strain

Department of Physics and Astronomy, University of Glasgow, Glasgow G12 8QQ, Scotland, United Kingdom
(October 25, 2018)

We compare two advanced designs for gravitational-wave antennas in terms of their ability to detect two possible gravitational wave sources. Spherical, resonant mass antennas and interferometers incorporating resonant sideband extraction (RSE) were modeled using experimentally measurable parameters. The signal-to-noise ratio of each detector for a binary neutron star system and a rapidly rotating stellar core were calculated. For a range of plausible parameters we found that the advanced LIGO interferometer incorporating RSE gave higher signal-to-noise ratios than a spherical detector resonant at the same frequency for both sources. Spheres were found to be sensitive to these sources at distances beyond our galaxy. Interferometers were sensitive to these sources at far enough distances that several events per year would be expected.

I. INTRODUCTION

The experimental effort to detect gravitational radiation has advanced substantially since its beginnings in the early 1960's [1]. Two different techniques, resonant-mass antennas and interferometers, have been developed over the years, but in the last decade construction has begun on long baseline interferometers designed for very high sensitivity.

In previous work [2] the sensitivity of these two technologies were compared using models of potential sources of gravitational waves. In that work, different diameter spherical, resonant-mass antennas [3] were compared with the expected sensitivity of initial LIGO [4] because it was plausible that both detectors could be in operation in the early years of the 2000 decade. Generally, LIGO was found to be more sensitive to these sources, especially the inspiraling binary neutron stars. However, at higher frequencies, spheres were shown to provide extra sensitivity within a restricted bandwidth. These higher frequencies, about 700 Hz to 5000 Hz, are where the gravitational waves from binary neutron star coalescence, rapidly rotating stellar cores, and other sources [13] are found.

Although gravitational wave sources occur at many different frequencies and amplitudes, binary neutron star inspirals emit gravitational waves at frequencies accessible to Earth-based interferometers, a few to a few hundred Hertz. Neutron star binaries also have an amplitude and event rate that makes it plausible that advanced interferometers will detect one or more a year [11]. At these frequencies, the neutron stars are many times their own radius apart from each other and act as point masses. This makes analytically predicting the waveform possible, but also means that the details of the neutron star composition (equation of state, radius, magnetic field, etc.) will not effect the waveform. When compact bodies such as neutron stars are close enough together that the gravitational radiation being given off carries information about their structure, the frequency is higher (typically above 700 Hz) and the amplitude is lower. This is true of the internal motion of compact bodies as well, such as the core collapse of a supernova. Determining astrophysically interesting parameters from these higher frequency waveforms will be a major goal of gravitational wave astronomy once the first detections have occurred and may require detectors specialized for higher frequency response.

Progress with interferometers and delays with spherical antennas make it more relevant now to compare spheres and a more advanced interferometer. One possible upgrade of LIGO would include an additional mirror at the output

*Current address: LIGO Project, Massachusetts Institute of Technology, Room NW17-161, 175 Albany Street, Cambridge, Massachusetts, 02139

†Permanent address: Harvard-Smithsonian Center for Astrophysics, 60 Garden Street, Cambridge, Massachusetts, 02138

port, which allows for signal recycling [5] or resonant-sideband extraction (RSE) [6]. These techniques allow the frequency of peak response to be selected over a wide range and the bandwidth of the response to be controlled. Such an upgrade would allow the advanced interferometer to operate with a similar strain spectrum as a spherical, resonant-mass antenna and have more sensitivity than other interferometer configurations at higher frequencies.

Here we compare the sensitivity of advanced LIGO, including RSE, with that of eight possible spherical antennas with different diameters to determine the effectiveness of each technology as a detector of high frequency gravitational radiation. The frequency of peak sensitivity and the bandwidth for the interferometer was chosen to correspond as closely as possible to the lowest quadrupole resonance of each of the spheres. Different peak-sensitivity frequencies for the interferometer are obtained by varying the position of the signal-extraction mirror (by a fraction of the wavelength of the laser light). The fractional bandwidth of a sphere is determined by the choice of transducer, and is typically below 20%. To reproduce this narrow bandwidth, the transmittance of the interferometer's signal-extraction mirror has been chosen to be relatively low. Once the interferometer has been matched to a given sphere, the sensitivity of the sphere and interferometer to different, high frequency, sources can be compared.

The signal-to-noise ratio for both the spheres and the interferometer was computed using the numerically simulated relativistic waveforms of two different gravitational wave (burst) sources: (1) the inspiral and eventual coalescence of a binary neutron star system, and (2) a rapidly rotating stellar core undergoing a dynamical instability [7,8]. Both of these sources are predicted to have high enough event rates that they could be detected by interferometers within the next ten years [4,9–11,13]

There are many other sources of gravitational waves that could provide interesting physical and/or astrophysical information. The stochastic background of gravitational radiation depends on conditions at the earliest times in the universe [14] and their detection would shed new light on cosmology. Searches for scalar radiation would allow for tests of gravity beyond the prediction of general relativity. Both interferometers and spheres may play a role in these experiments, but we did not consider these sources in this work.

II. METHOD

The spherical antennas were modeled using the same method as described in the previous paper [2]. The signal-to-noise ratio density was calculated for each sphere using the method of Price [15] as extended by Stevenson [16]. This involved calculating the signal-to-noise ratio density from the strain spectrum of each sphere. The parameters that entered the strain spectrum were chosen based, as much as possible, on optimistic extrapolations from values demonstrated in operating detectors.

Eight aluminum spheres were modeled with diameters of 3.25 m, 2.75 m, 2.35 m, 2.00 m, 1.70 m, 1.45 m, 1.25 m, and 1.05 m. The 3.25 m sphere weighs 50 tonnes and is the largest solid sphere which can reasonably be manufactured and transported. It may be possible to get larger radii spheres, and hence lower resonance frequencies, by building hollow spheres [17] but we did not consider these detectors. A lower frequency, hollow sphere will have advantages with lower frequency sources, especially the inspiral phase of the binary neutron star signal, but not with the higher frequency sources we considered here. Each sphere was modeled as having six, three-mode inductive transducers arranged in the TIGA geometry [3] which allows for omnidirectional sensitivity. The masses of the intermediate mass and the final transducer mass (see Fig. 1) were chosen to give a fractional bandwidth as large as possible for each sphere. The transducer was modeled as having a dual, superconducting quantum interference device (SQUID) as the first stage amplifier. SQUID amplifiers are currently in use on bar detectors [18,19]. A three-mode transducer is being developed for use on the Allegro antenna [20] and one has been successfully demonstrated on a test antenna [21].

The limiting noise in a spherical resonant mass detector comes from two sources; amplifier noise and thermal noise. The amplifier noise, which comes primarily from the sensing SQUID, can be separated into additive velocity noise and force noise. The additive velocity noise can be written as [2]

$$S_u(f) = N_n \hbar 2\pi f_0 / r_n, \quad (1)$$

where N_n is the noise number of the SQUID, \hbar is Planck's constant, f_0 is the resonant frequency of the sphere, and r_n is the noise resistance of the transducer. We assumed that the SQUID had quantum-limited noise, and hence a noise number equal to one. A quantum-limited SQUID suitable for use in a gravitational wave transducer has not yet been demonstrated, although the quantum limit has been reached in SQUIDs with low input impedance [22]. A noise number of 24 has been reached at 100 mK in a suitable SQUID when cooled on its own [23]. This noise, however, was found to increase significantly when placed in a transducer [24].

The noise resistance was calculated from

$$r_n = \kappa A_{\text{coil}} / (4\pi f_0), \quad (2)$$

where κ is an experimentally determined spring constant density given in Table I and $A_{\text{coil}} (= \pi (d_c/2)^2)$ is the area of the pick-up coils. The noise resistance limits the bandwidth of a sphere with three-mode transducers (when the masses are properly chosen) according to [15]

$$\delta_{\text{BW}} \sim (r_n / (2\pi f_0 m_s))^{1/5}, \quad (3)$$

where m_s is the effective mass of the sphere for impedance calculations. This effective mass is given by [16,25]

$$m_s = 5/6 \chi m_p \quad (4)$$

where $\chi = 0.301$ [25], m_p is the physical mass of the sphere, and the factor 5/6 is appropriate for six transducers in the TIGA arrangement [16]. The amplifier velocity noise is shown in Fig. 2 graphed as a strain spectrum.

The force noise from the SQUID is ultimately detected as motion, and therefore must be converted by the mechanical transfer function of the antenna. The output noise can be written [2]

$$S_{f,\text{out}}(f) = N_n \hbar 2\pi f_0 r_n |y_{22}(f)|^2, \quad (5)$$

where the admittance matrix element $y_{22}(f)$ for a sphere with three-mode transducers can be written

$$\begin{aligned} y_{22}(f) = & -2\pi f i (c_1 + c_2 + c_s - 4\pi^2 f^2 (c_2 (c_1 + c_s) m_1 + (c_1 + c_2) c_s m_s) + \\ & 16\pi^4 f^4 c_1 c_2 c_s m_1 m_s) / (-1 + 4\pi^2 f^2 (c_1 m_1 + c_s m_1 + c_1 m_2 + c_2 m_2 + \\ & c_s m_2 + c_s m_s) + 16\pi^4 f^4 (c_1 c_2 m_1 m_2 - c_2 c_s m_1 m_2 - c_1 c_s m_1 m_s - \\ & c_1 c_s m_2 m_s - c_2 c_s m_2 m_s) + 64\pi^6 f^6 c_1 c_2 c_s m_1 m_2 m_s). \end{aligned} \quad (6)$$

In the above, c_1 is the reciprocal spring constant k_1 for the spring separating the sphere from the intermediate mass of the transducer, c_2 is the reciprocal spring constant k_2 for the spring separating the intermediate mass from the transducer mass, c_s is the reciprocal spring constant k_s of the effective spring separating the effective mass of the sphere from mechanical ground, m_1 is the mass of the intermediate mass of the transducer, m_2 is the mass of the transducer mass, and m_s is the effective mass of the sphere for the lowest quadrupole mode. The masses and springs in the transducer are shown in Fig. 1. The spring constants can be written for each stage in the transducer ($j=1,2$, or s)

$$k_j = (2\pi f_0)^2 m_j + i (2\pi f) (2\pi f_0) m_j / Q_j, \quad (7)$$

where Q_j is the quality factor of the appropriate stage of the transducer and sphere. The Q 's depend on composition, temperature, and the connections between the masses and springs. The amplifier force noise is shown in Fig. 2 graphed as a strain spectrum .

The thermal noise of the sphere can be written [2]

$$S_{\text{sph,therm}} = 2k_B T \Re(y_{22}(f)), \quad (8)$$

where T is the physical temperature of the sphere. We modeled the antenna as having a T of 50 mK, although 95 mK is the lowest a bar has been cooled at equilibrium [26,27]. The term $\Re(y_{22}(f))$ depends on the Q 's, with higher Q 's resulting in lower thermal noise. The sphere and intermediate mass were modeled in aluminum and the transducer mass was modeled in niobium. Each of the mechanical Q 's was modeled as 40×10^6 [28–30]. Depending on the design of the transducer, the final Q can be degraded by the addition of loss from electrical coupling to the SQUID circuit [31]. The sphere's thermal noise is shown in Fig. 2 graphed as a strain spectrum.

All of the noise sources for the sphere were then combined to determine the total noise;

$$S_{\text{tot}}(f) = S_u(f) + S_{f,\text{out}}(f) + S_{\text{sph,therm}}. \quad (9)$$

This total noise is shown, along with each component, in Fig. 2 graphed as a strain spectrum.

The gravitational wave signal is applied as force on the spherical antenna, but is read out as velocity of the transducer mass. Thus, before a signal can be compared to these noise sources, the gravitational strain must be converted to a force and be passed through the admittance matrix of the sphere-transducer system. The comparable signal can be written [2]

$$\Sigma(f) = \frac{\pi Y^{5/2} \Pi m_s}{f_0^3 \rho^{3/2}} f^2 |y_{21}(f) h(f)|^2, \quad (10)$$

where Y is Young's modulus for the sphere material, ρ is the density of the sphere material, Π is the reduced cross section of the sphere and equals 0.215 for the lowest quadrupole mode [25], $h(f)$ is the frequency-domain amplitude of the gravitational wave, and the admittance matrix element $y_{21}(f)$ can be written

$$\begin{aligned} y_{21}(f) = & 2\pi f c_s i / (-1 + 4\pi^2 f^2 (c_1 m_1 + c_s m_1 + c_1 m_2 + c_2 m_2 + c_s m_2 + c_s m_s)) \\ & - 16\pi^4 f^4 (c_1 c_2 m_1 m_2 + c_2 c_s m_1 m_2 + c_1 c_s m_1 m_s + c_1 c_s m_2 m_s + c_2 c_s m_2 m_s) \\ & + 64\pi^6 f^6 c_1 c_2 c_s m_1 m_2 m_s). \end{aligned} \quad (11)$$

Table I shows all the parameters used in the sphere model.

The interferometer was modeled using a slightly modified version of the **BENCH** program [32]. The noise in the interferometer is dominated by three types of noise; seismic, thermal, and optical readout noise. Each noise source was modeled using parameters from the advanced LIGO white paper [33], which is scheduled to be implemented in 2005. The corresponding advanced interferometer is scheduled to begin taking data in 2007. A schematic drawing of LIGO with RSE is shown in Fig. 4

Seismic noise is expected to dominate the advanced LIGO noise budget at low frequencies. To reduce the effect of seismic noise, each element of the interferometer will be supported by a four-stage suspension which in turn is supported from a vibration isolation stack. This vibration isolation will consist of two stages of six-degree of freedom isolation. It will use a combination of active and passive isolation with an external hydraulic actuation stage. The isolation was designed to make seismic noise negligible compared to other noise sources above some f_{seismic} , expected to be 10 Hz. In the model, seismic noise was made extremely high below 10 Hz and vanishingly small above this frequency.

Thermal noise will be the dominant noise source in advanced LIGO in the intermediate frequency band above 10 Hz. This noise can be divided into two types; thermal noise from the internal degrees of freedom of the interferometer mirrors, and thermal noise from the suspension that supports the mirrors. The mirrors are planned to be made of m-axis sapphire, 28 cm in diameter and 30 kg in mass. Sapphire has been found to have much lower internal friction than fused silica [34,35], which is used in initial LIGO. However, sapphire suffers from much higher thermoelastic damping than silica [36].

The internal mode thermal noise from the sapphire mirror comes from structural damping and thermoelastic damping. The noise from structural damping can be found from the loss angle ϕ by

$$S_{\text{str}}(f) = \frac{1}{L^2} \frac{8k_B T \phi}{\pi f} (C_1 + C_2), \quad (12)$$

where k_B is Boltzmann's constant, T is the temperature, f is the frequency, and L is the interferometer arm length. The constants C_1 and C_2 are the overlap between the normal modes of the mirrors and the gaussian-profile laser, which has a width w_1 at the input mirror and w_2 at the end mirror. They are found from [37,38]

$$\begin{aligned} C_j = & \frac{(1 - \sigma^2)}{\pi r Y} \sum_{i=1}^N \left(\frac{\exp\left(-(\zeta_i w_j / (2r))^2\right)}{\zeta_i J_0(\zeta_i)^2} \frac{(1 - \exp(-4\zeta_i h/r) + 4\zeta_i h/r \exp(-2\zeta_i h/r))}{(1 - \exp(-2\zeta_i h/r))^2 - 4(\zeta_i h/r)^2 \exp(-2\zeta_i h/r)} \right) \\ & + \frac{r^2}{6\pi h^3 Y} \left(h^4 / r^4 + 12\pi h^2 \sigma \sum_{i=1}^N \frac{\exp\left(-(\zeta_i w_j / (2r))^2 / 2\right)}{\zeta_i^2 J_0(\zeta_i)} \right. \\ & \left. + 72(1 - \sigma) \left(\sum_{i=1}^N \frac{\exp\left(-(\zeta_i w_j / (2r))^2 / 2\right)}{\zeta_i^2 J_0(\zeta_i)} \right)^2 \right). \end{aligned} \quad (13)$$

where σ is the Poisson ratio of the mirror material, Y is it Young's modulus, r is the radius of the mirror, ℓ is the thickness of the mirror, w is the Gaussian beam width of the laser at the mirror, ζ_i are the zeros of the first order Bessel function J_1 , and J_0 is the zeroth order Bessel function. The value of ϕ used is the lowest value measured for a piece of sapphire [34]. The thermal noise effects of making a sapphire piece into a mirror are under study, but the polishing and especially coating of the mirror are expected to cause some excess loss [39,40].

Thermoelastic damping also contributes to thermal noise from the mirrors. It is found, in the limit of large mirror diameter, from [36]

$$S_{th}(f) = \left(\frac{(1 + \sigma) \alpha T}{\pi f L C_V \rho} \right)^2 \frac{16 \kappa k_B}{\sqrt{\pi}} (1/w_1^3 + 1/w_2^3), \quad (14)$$

where α is the thermal expansion coefficient, C_V is the heat capacity at constant volume, ρ is the density, and κ is the thermal conductivity. Fused silica is available as a back up material which does not have as much thermoelastic loss and has recently been shown to have a ϕ as low as 1.8×10^{-8} in certain circumstances [41].

Thermal noise from the suspension, which supports the mirrors below the vibration isolation stack, will be reduced in advanced LIGO by replacing the steel slings with fused silica ribbons. Fused silica has much less internal friction than steel [42–44], although with ribbon geometry surface loss limits the achievable dissipation [43,45]. Thermal noise from a ribbon suspension with surface loss has recently been considered [45] and the results give thermal noise, expressed as gravitational wave stress squared per Hertz, as

$$S_{\text{susp}}(f) = 32k_B T \phi_{\text{dil}} g \left/ L^2 \left(L_{\text{sus}} m 2\pi f \left(\left((2\pi f)^2 - \omega_{\text{pen}}^2 \right)^2 + \omega_{\text{pen}}^4 \phi_{\text{dil}}^2 \right) \right) \right., \quad (15)$$

where g is the acceleration due to gravity, L_{sus} is the length of the suspension, m is the mass of the mirror, ω_{pen} is the angular frequency of the pendulum mode, and ϕ_{dil} is the diluted loss angle. This diluted loss angle is defined as

$$\phi_{\text{dil}} = \sqrt{Y / (12\gamma\sigma L_{\text{sus}}^2)} d (\phi_{\text{th}} + \phi_{\text{int}}), \quad (16)$$

where Y is Young's modulus for the ribbon material, γ is the ratio of stress in the ribbon to its breaking stress, σ is Poisson's ratio for the ribbon material, d is the ribbon thickness, ϕ_{th} is the loss angle due to thermoelastic damping, and ϕ_{int} is the loss angle due to internal friction in the ribbon. Thermoelastic damping in ribbons is found from [46]

$$\phi_{\text{th}} = \frac{Y\alpha^2 T}{C} \frac{2\pi f \tau_d}{1 + (2\pi f)^2 \tau_d^2}, \quad (17)$$

where α is the thermal expansion coefficient of the ribbon material, C is the heat capacity per unit volume, and τ_d is the time constant for thermal diffusion which in ribbons is given by

$$\tau_d = d^2 / (\pi^2 D), \quad (18)$$

with D being the thermal diffusion coefficient for the ribbon material. The internal friction in a thin ribbon is given by [43]

$$\phi_{\text{int}} = \phi_{\text{bulk}} (1 + 6d_s/d), \quad (19)$$

where ϕ_{bulk} is the loss angle in the bulk of the ribbon material, and d_s is the dissipation depth that characterizes the excess loss arising from the surface of the ribbon. The numbers for ϕ_{bulk} and d_s in Table II represent possibly achievable values, lower values for both have been observed [41,47]. Determining realizable values for these parameters in advanced LIGO is an area of intense research.

Optical readout noise in the interferometer can be evident at any frequency in the LIGO detection band. This noise source has two separate components: radiation pressure noise from the pressure exerted on the mirrors by the laser and shot noise from the inherent granularity (photons) of the laser light. These two noise sources are complementary to each other, both depend on the laser power. Recently, optical readout noise in a signal-recycled interferometer has been considered from a fully quantum mechanical perspective [48]. The noise spectrum does differ from the one we calculate here, but the difference at high frequencies in a narrowband configuration are negligible.

The optical power stored in the interferometer is an important parameter for the optical readout noise. There are a number of optical cavities in LIGO formed by the different mirrors (input mirrors, end mirrors, power recycling mirror, signal recycling mirror, etc.) and each one stores a different amount of power. It is convenient to quote a single power, the power incident on the beam splitter, and then calculate the power in different cavities in terms of this single value. The power at the beam splitter is proportional to the power out of the laser, P , through the power recycling factor

$$P_{bs} = G_{pr} P, \quad (20)$$

which is found from

$$G_{pr} = 1 / (2N\beta + \alpha_{BS}), \quad (21)$$

where α_{BS} is the fractional power loss at the beam splitter, β is the fractional power loss at each mirror, and N is the number of bounces that the light makes in each arm, on average. In Fabry-Perot cavities, in the large finesse limit, the value N can be found from the finesse,

$$N = 2\mathcal{F}/\pi, \quad (22)$$

where the finesse \mathcal{F} is found from the amplitude transmittance of the input mirror, t_1 :

$$\mathcal{F} = 2\pi/(t_1^2 + 2\beta). \quad (23)$$

These equations taken together with the parameters in Table II give the power at the beam splitter,

$$P_{bs} = 9.3 \text{ kW}. \quad (24)$$

This power must be kept from being too high because absorption of light in the transmitting mirrors, beam splitter, and coatings can lead to thermal lensing. The acceptable thermal lensing limit can be calculated from (including a factor of 2 safety margin) [49]

$$P_{\max} \approx \frac{\kappa}{2 \text{ dn/dT}} \frac{\lambda}{1.43A_g t_{BS} + 1.3A_g \ell + \frac{1}{2} N a_{\text{coat}}}, \quad (25)$$

where κ is the thermal conductivity of the substrate material, dn/dT is the change in index of refraction of the substrate with temperature, A_g is the optical absorption of the substrate, and a_{coat} is the relative absorption of the optical coating. Using the numbers in Table II, this maximum allowable power is

$$P_{\max} = 750 \text{ W}. \quad (26)$$

In order to realize the higher power in Eq. (24), a correction scheme must be utilized that increases P_{\max} by a factor of at least 12.4 for sapphire optics. Research is underway to have such a correction scheme available for advanced LIGO [33].

Both parts of the optical readout noise depend on the response of the coupled cavity system in the interferometer. This response can be described by the transfer function between the amplitude of the light in the arm cavity and the amplitude of light that enters through the input mirror in each sideband [48]:

$$G_{0,1} = 1 - r_1 r_2 \exp(i\tau_a 2\pi f) - r_1 r_3 \exp(i(\tau_s 2\pi f + \delta)) + r_2 r_3 \exp(i((\tau_a + \tau_s) 2\pi f + \delta)), \quad (27)$$

$$G_{0,2} = 1 - r_1 r_2 \exp(-i\tau_a 2\pi f) - r_1 r_3 \exp(-i(\tau_s 2\pi f + \delta)) + r_2 r_3 \exp(-i((\tau_a + \tau_s) 2\pi f + \delta)) \quad (28)$$

where r_1, r_2 , and r_3 are the amplitude reflection coefficients at the input mirror, the end mirror, and the signal recycling mirror, respectively, $\tau_a (= 2L/c)$ is the light transit time between the input mirror and the end mirror, $\tau_s (= 2L_{\text{rec}}/c)$ is the light transit time between the input mirror and the signal recycling mirror with L_{rec} the length of this signal recycling cavity, and δ is the phase accumulated by the reflected light coming off the signal recycling mirror due to its position. The amplitude reflection coefficient for the input mirror can be found from

$$r_1^2 = 1 - t_1^2 - \beta. \quad (29)$$

The amplitude reflection coefficient for the end mirror can be found from

$$r_2^2 = 1 - \beta. \quad (30)$$

The amplitude reflection coefficient for the signal recycling mirror, r_3 , is a tunable parameter as is the accumulated phase, δ .

Radiation pressure noise is largest at low frequencies and, for initial LIGO, is masked by other low frequency noise (seismic and suspension thermal noise) [4]. In advanced LIGO, the suspension thermal noise may be low enough that radiation pressure is important, but it will still not be the dominant noise source. Radiation pressure was modeled by

$$S_{\text{rad}}(f) = 32P_{bs} 2\pi f \lambda \hbar t_1^4 t_3^2 r_2^2 (1/|G_{0,1}| + 1/|G_{0,2}|)^2 / ((1 - r_1 r_2) (2\pi f)^2 c m L)^2, \quad (31)$$

where f_λ is the frequency of laser light and t_3 is the amplitude transmittance of the signal recycling mirror.

Shot noise from the laser is the dominant noise source at high frequencies for initial LIGO, and this will continue for advanced LIGO. This noise source was modeled by

$$S_{\text{shot}}(f) = \left(\frac{f(1 - r_1 r_2)}{f_\lambda \sin(\pi f \tau_a) t_1^2 r_2 t_3 (1/|G_{0,1}| + 1/|G_{0,2}|)} \right)^2 \frac{4\pi f \hbar}{\eta P_{bs}}, \quad (32)$$

where η is the quantum efficiency of the photodiode.

All of these noise sources were combined to create the total noise curve for advanced LIGO;

$$S_{\text{tot}}(h) = S_{\text{seis}} + S_{\text{int}} + S_{\text{susp}} + S_{\text{shot}} + S_{\text{rad}}. \quad (33)$$

To produce a numerical estimate of the noise and then a signal-to-noise ratio for a given source, values must be provided for all the parameters that go into Eq. (33). We used values from the advanced LIGO white paper [33] as much as possible. The values chosen for all relevant parameters are shown in Table II. A graph of advanced LIGO's noise compared with spheres is shown in Fig. 3.

The masses in LIGO are designed to be as close to being in local free fall in the sensitive direction as possible. Therefore, the strain from a passing gravitational wave directly gives the change in position of the mirrors. The comparable signal, similar to Eq. (10), for an interferometer reads

$$\Sigma(f) = |h(f)|^2. \quad (34)$$

Using Eqs. 9 and 33 for the noise of a sphere and interferometer and Eqs. 10 and 34 as the comparable signals, the signal-to-noise ratio density for each detector can be found from

$$\sigma(f) = \Sigma(f) / S_{\text{tot}}(f). \quad (35)$$

Integrating the signal-to-noise ratio density gives the signal-to-noise ratio;

$$S/N = \left\langle \int_{-\infty}^{+\infty} \sigma(f) df \right\rangle, \quad (36)$$

where the angle brackets, $\langle \dots \rangle$, denote averaging over gravitational wave polarization and direction. This results in a factor of 1/5 [13] for interferometers and a factor of 1 for spheres, as spheres are always optimally oriented. This value, S/N , is the figure of merit for a gravitational wave detector and will be used to compare the effectiveness of these two different approaches to the different astronomical sources.

To compare the sensitivities of the the antennas, it is useful to calculate the strain spectral density $\tilde{h}(f)$,

$$\tilde{h}(f) = \sigma(f) / |h(f)|^2. \quad (37)$$

This quantity incorporates both the total noise of the detector and the cross section. It is the strain spectrum that is shown in Figures 2,3 and 5.

III. SOURCES

One category of sources for gravitational radiation at high frequencies (above 700 Hz) is from internal motion of compact bodies such as neutron stars. The coalescence and merger of neutron stars as well as neutron star formation in collapsing stellar cores are promising sources of detectable gravitational waves. Detecting and analyzing these waves promises to teach us a great deal about the physics of strong gravitational fields and extreme states of matter [9]. Because of the high rotational velocities and strong gravitational fields present in such compact objects, numerical simulations must include the effects of general relativity to model the system dynamics realistically enough for use in analysis of the data from antennas. To accomplish this goal, a three-dimensional Smoothed Particle Hydrodynamics code [54] has been modified to include the General Relativistic "back reaction" [8,7]. The gravitational radiation from these systems is calculated in the quadrupole approximation.

The component stars of a widely separated binary neutron star system will spiral together due to orbital energy losses by gravitational radiation reaction, and eventually coalesce [10,55,56]. Because neutron stars have intense self-gravity, as they inspiral they do not gravitationally deform one another significantly until several orbits before final coalescence [9]. When the binary separation is comparable to a neutron star radius, tidal distortions become significant, hydrodynamical effects become dominant, and coalescence occurs in a few orbits.

The inspiral phase of the evolution comprises the last several thousand binary orbits and covers the frequency range $f \sim 10 - 1000$ Hz. The final coalescence is believed to emit its gravitational waves in the kilohertz frequency band range $800 \text{ Hz} < f < 2500 \text{ Hz}$ [9,57-59]. The observation of the inspiral and coalescence waveforms will reveal information about the masses and spin angular momenta of the bodies, the initial orbital elements of the system, the neutron star radii and hence the equation of state for nuclear matter [9,57-59].

Theoretical estimates of the formation rates for binary neutron star systems—with tight enough orbits to merge due to gravitational radiation within a Hubble time—can be obtained from empirical rate estimates based on the observed sample [60]. The most recent study gives a Galactic lower and upper limit of $2 \times 10^{-7} \text{ yr}^{-1}$ and $\sim 6 - 10 \times 10^{-6} \text{ yr}^{-1}$, respectively [11]. Alternatively, by modeling the evolution of the Galaxy’s binary star population, the best estimates for coalescence events have been estimated to be as high as 3×10^{-4} coalescences per year in our galaxy, and several per year out to a distance of 60 Mpc [9]. We have used 15 Mpc as an optimistic estimate and 200 Mpc as a pessimistic estimate of the distance antennas will need to look to get about one event per year for this source.

For the simulation presented here, equal mass component stars are used. Each star is assumed to have a total mass of $M_t = 1.4 M_\odot$, and equatorial radius, $R_{\text{eq}} = 10 \text{ km}$, where M_\odot is one solar mass. The star is modeled as a differentially rotating axisymmetric fluid which use a polytropic equation of state,

$$P = k\rho^\gamma \tag{38}$$

$$= k\rho^{1+1/n}, \tag{39}$$

where k is a constant that measures the specific entropy of the material and n is the polytropic index. The value $n = 1$ is used to simulate cold nuclear neutron star matter. Each star rotates counterclockwise about the z -axis with an equatorial surface speed of approximately $0.083 c$ [7].

Since the binary system spirals together due to energy and angular momentum losses via the emission of gravitational radiation, as the orbit decays, it circularizes radially. Thus, it is a good approximation to assume a circular orbit provided the system is expected to have existed for some time [61]. The component stars used in the simulation are initially placed on a sufficiently wide circular orbit (center of mass distance is 40 km) so that tidal effects are negligible [62,63]. Because of the large initial separation, the stars start out in the point mass regime, and as a result, their waveforms can be compared directly to the theoretical point-mass inspiral for two neutron stars [64].

Although spin-orbit misalignment in coalescing compact binaries can change the amplitude and modulation of the gravitational radiation waveforms, this effect is believed unimportant in the case of a binary neutron star system [12]. Thus, in the numerical simulation, the orbital and spin angular momentum vectors were assumed to be aligned. If the magnetic axis is not aligned with the rotation axis, the ejecta from the coalescence can be trapped within the field [65]. The evolution of the magnetic field configuration during the final inspiral phase of neutron star binaries may have significant effects on the frequency and tidal distortion of the coalescence, and hence on the gravitational waveforms [66]. The inclusion of this effect is the subject of current research [67].

A series of snapshots of the inspiral and coalescence of the neutron stars along with a graph of the waveform generated is shown in Figure 6. The waveform differs noticeably from ones generated with purely Newtonian gravity [62]. The gravitational wave peak due to the bar formed during coalescence, seen in Fig. 6(A)(d), is at a much higher frequency; 3700 Hz with General Relativistic back reaction compared to 2500 Hz in the Newtonian case. This peak is also broader and less pronounced in the General Relativistic simulation than in the Newtonian.

Rotational instability during the gravitational collapse of a massive star’s degenerate core has long been considered an interesting possible source of gravitational radiation. A typical scenario in which such a mechanism can operate is the collapse of a rapidly rotating stellar core that has exhausted its nuclear fuel and is prevented from collapsing to neutron star size by centrifugal forces. If a significant amount of angular momentum remains in an initially axisymmetric core, collapse may be slowed or temporarily stalled by centrifugal forces associated with rotation. If the core’s rotation is large enough to strongly flatten the core before, or as it reaches neutron-star density, then an instability is likely to break the core’s axial symmetry [9,68,69]. The growth of such global rotational instabilities provides a means for transport of angular momentum out of the core into the surrounding envelope by transforming the core into a bar-like configuration rotating about the short axis, shedding mass in a spiral pattern, thereby allowing collapse to continue to a supernova [7,8,69–73].

The strength of the gravitational waves from such a supernova depends crucially on degree of non-sphericity during the collapse, and somewhat on the speed of collapse. If a substantial fraction of the collapsing object’s angular momentum goes into generating gravitational rather than hydrodynamical waves then the gravitational waves generated may be nearly as strong as those generated from a coalescing binary [13].

The event rates of Type II Supernovae are fairly well known from observations [13]. In our Galaxy, Type II Supernovae occur approximately once every 40 years, and several per year out to the distance of the Virgo Cluster of Galaxies (about 10 Mpc). Beyond this point, the rate increases roughly as the cube of the distance, where by $\sim 300 \text{ Mpc}$ the supernova rate becomes $\sim 10^4$ per year [13,70]. Although it is unclear what fraction of collapsing cores may undergo an instability, if only $\sim 1/1000$ or $1/10^4$ do so, this phenomena could be a significant source of detectable gravitational radiation [9].

For the simulation presented here, the pre-collapsed stellar core is modeled as a differentially rotating, compressible, axisymmetric fluid which uses a polytropic equation of state. The stellar core is assumed to have collapsed to the point where centrifugal hangup occurs, reaching near neutron star densities (polytropic index $n = 0.5$) prior to the

onset of a global dynamical instability. To maximize relativistic effects, the core is assumed to have a total mass of $M_t = 1.4M_\odot$, and equatorial radius, $R_{\text{eq}} = 10$ km. However, the collapse phase itself is not simulated. The star rotates counterclockwise about the z -axis at an equatorial surface speed of approximately $0.122c$ [7,8]. The event was modeled as occurring at a distance of 1 Mpc as an optimistic estimate of the distance necessary for antennas to see roughly one event per year [9]. A series of snapshots of the evolution along with a graph of the waveform used is shown in Figure 7.

Strongly magnetized neutron stars are expected to form at the end of Type II Supernova collapse. For sufficiently strong fields, misalignment between the rotation and magnetic axes can distort the star by trapping the ejecta within the field [65]. This can cause a reduction in the angular momentum in a rapidly rotating core through magnetic braking, which can remove several orders of magnitude from the initial angular momentum over long enough time scales [74]. The inclusion of magnetohydrodynamical effects into the existing numerical models will have significant consequences on the stability and subsequent evolution of the post-collapsed object [67].

IV. CALCULATIONS AND RESULTS

We used Eq. 36 to find signal-to-noise ratios for both spherical resonant mass detectors and the advanced LIGO interferometer with RSE detecting the binary neutron star and the rapidly rotating stellar core sources. For each source, we calculated seventeen signal-to-noise ratios; one each for a sphere and interferometer configuration at eight different frequencies plus one for advanced LIGO in a broadband mode. Although signal-to-noise ratio is ultimately the figure of merit for a gravitational wave antenna, the comparison of strain spectra (as in Fig. 3) gives a full understanding of the relative merits of the two detectors. We present the signal-to-noise ratio calculations to show how each antenna performs astronomically. Comparisons between the two instruments can be done solely on the basis of noise performance and cross section.

The frequencies were set by the choice of diameter for the spheres. The largest sphere, 3.25 m in diameter, has a mass of 50 tonnes. The smallest sphere chosen has a diameter of 1.05 m. Any smaller, and the cross section for gravitational wave detection (implicit in Eq. 10) becomes too small for any realistic sources. The resonant frequencies of these spheres are given by [3]

$$f_0 = 1.62/(\pi d_{\text{sph}})\sqrt{Y/\rho}, \quad (40)$$

where d_{sph} is the diameter of the sphere, Y is the Young's modulus of the sphere material, and ρ is the density of the sphere material. This choice of diameters, then, allows for sensitivity between 795 Hz and 2461 Hz, see Table III.

The most sensitive frequency of the interferometer's noise spectrum was adjusted by changing the position of the signal recycling mirror. A change in position less than the wavelength of the laser light results in a change in phase δ in Eqs. (27) and (28). This, then, changes the frequency characteristic of the shot noise.

The appropriate δ was found from setting the derivative of the shot noise with respect to frequency at the resonance frequency of the sphere equal to zero. This insures the minimum of the shot noise, which is the dominant noise source at frequencies above 500 Hz, will be at the same frequency as the sphere's most sensitive point. Since the frequency dependence of the shot noise is all in the function

$$|G_0(f)| = 1/(1/|G_{0,1}(f)| + 1/|G_{0,2}(f)|), \quad (41)$$

this condition can be written

$$\begin{aligned} 0 &= \partial|G_0(f)|/\partial\delta \\ &= (r_3(r_1(1+r_2^2)\sin(2\pi f\tau_s+\delta) - r_2(r_1^2\sin(2\pi f(\tau_s-\tau_a)+\delta) + \sin(2\pi f(\tau_a+\tau_s)+\delta))) \\ &\quad / (2(1+r_1^2r_2^2+r_1^2r_3^2+r_2^2r_3^2-2r_1r_2(1+r_3^2)\cos(2\pi f\tau_a)-2r_1(1+r_2^2)r_3\cos(2\pi f\tau_s+\delta) \\ &\quad +2r_1^2r_2r_3\cos(2\pi f(\tau_s-\tau_a)+\delta)+2r_2r_3\cos(2\pi f(\tau_a+\tau_s)+\delta))^{1/2}). \end{aligned} \quad (42)$$

Using this equation, the appropriate phase shifts for the signal recycling cavity were found, and are presented in Table III.

The bandwidth of the sphere is determined by the impedance matching between the sphere and the SQUID amplifier. With a three stage transducer, this bandwidth is given by

$$\delta_{\text{BW}} = \sqrt{m_2/m_1}, \quad (43)$$

where δ_{BW} is the fractional bandwidth of the sphere in the lossless limit [15]. For the choices of masses in the transducer from Table I, this bandwidth becomes

$$\delta_{\text{BW}} = 10\%. \quad (44)$$

In the interferometer, the bandwidth of the high frequency response is determined by the reflectivities of the input mirror and the signal recycling mirror, r_1 and r_3 respectively. The bandwidth of both the sphere and of the interferometer was calculated from

$$\delta_{\text{BW}} = 1/(2f_0) \left(\int S_{\text{tot}}(f) df \right)^2 / \int S_{\text{tot}}^2(f) df. \quad (45)$$

To adjust the bandwidth of LIGO to better approximate the noise spectrum of a sphere, the values t_1 and t_3 were then chosen to get the minimum bandwidth possible. The values used for all frequencies were $t_1 = \sqrt{0.03}$ and $t_3 = \sqrt{0.005}$. The bandwidth turns out to be higher than 10%, the sphere's bandwidth, for all peak frequencies. Decreasing t_3 leads to losses dominating over the transmittance which limits the peak sensitivity.

The resulting signal-to-noise ratios for the spheres and interferometer configurations are shown in Fig. 8 for the binary neutron star inspiral and coalescence, in Fig. 9 for the inspiral and coalescence phases separately, and in Fig. 10 for the rapidly rotating stellar core undergoing a dynamical instability. We also calculated signal-to-noise ratios for the sources interacting with LIGO in a broadband configuration optimized for binary neutron star inspiral. This involves changing the input transmittance, t_1^2 to 0.005, the signal recycling mirror transmittance, t_3^2 to 0.05, and the accumulated phase δ to 0.09. These signal-to-noise ratios are shown in the same figures with a dotted line.

V. CONCLUSIONS

Interferometers utilizing resonant sideband extraction can be more sensitive than the most sensitive spheres, both on and off resonance. This condition remains true even when the effects of random polarization and direction of the gravitational wave are accounted for. Spheres are always optimally oriented towards incoming waves. Figures 8 and 10 indicate that this greater sensitivity translates into significantly higher SNR's for the interferometer over spheres for the two sources we considered.

These two figures show how sensitive each technology is to the two sources. A properly sized sphere can detect the inspiral signal of a binary neutron star system at a distance of 15 Mpc. This is far enough to reach the nearer sections of the Virgo cluster of galaxies. According to optimistic estimates [2,10] this may be enough to detect one event per year. Advanced LIGO can see binary neutron star events out to 200 Mpc with a single detector, the most likely distance necessary to see multiple events per year [10]. Advanced LIGO will also be able to see rapidly rotating stellar core events at a far enough distance to detect multiple events a year. Depending on the size of the sphere, resonant mass technology may also have enough sensitivity to see one or more rapidly rotating stellar core events a year as well.

Detecting the coalescence phase of the binary neutron star event would provide information about the structure of these stars (e.g., the equation of state and the equatorial radius). Advanced LIGO properly tuned to a high frequency, narrowband configuration provides the highest signal-to-noise ratio for this source. In this mode, Advanced LIGO has enough sensitivity to detect the coalescence waveform at a distance of 100 Mpc. This may be enough to actually see such an event during the expected lifetime of Advanced LIGO. Advanced LIGO tuned to 1292 Hz, where the highest signal-to-noise ratio is obtained, is mostly sensitive to the early stages of coalescence. Choosing both a sphere radius of 70 cm and a phase, δ , for the interferometer of 0.04613, allows these antennas to be tuned to the 3700 Hz of the rotating bar peak. The SNR for the sphere at this frequency is only 4.5×10^{-2} at 15 Mpc. Advanced LIGO has a SNR of 6.39 at this distance, but event rate predictions are pessimistic about a coalescence happening this close.

A comparison of the signal-to-noise ratios found in the previous paper [2] for binary neutron star events with Figures 8 and 10 shows that the addition of the gravitational wave back reaction to the model does change the waveform of the coalescence phase of the binary neutron star evolution. It is important for deciding the best configuration of advanced LIGO to know the details of the coalescence waveform. Other effects, notably inclusion of the magnetic fields in the neutron stars and post-Newtonian corrections [78], may change all these waveforms, especially for the coalescence and the rapidly rotating stellar core events. We have used the best available models to predict the gravitational radiation but further improvements are probable and our results should be seen in this light.

Despite the sensitivity advantages of interferometers, spheres do have benefits which should allow them to find a niche in the field of gravitational wave detection. Having simultaneous detection of a single event by two completely different technologies will help confirm signals with marginal SNR's; a near certainty in the early years of gravitational

wave astronomy. Having a sphere near to an interferometer site will also allow for correlated searches for stochastic backgrounds of cosmological gravitational waves [75,76]. It is conceivable that such pairing may occur in Louisiana between LIGO and Louisiana State University and in Italy between Virgo and an Italian sphere.

Spheres may be particularly well suited for detecting scalar radiation [77,79,80] because of their symmetry properties. This would allow for exploration of gravity beyond the predictions of general relativity. The comparatively low cost of spherical antennas in relation to interferometers could allow for construction of more individual detectors which are located more widely around the globe. The decades of experience working with bar detectors will provide useful background for sphere projects. Operation in conjunction with the interferometer network, an array of spherical detectors will be a valuable asset to the worldwide effort to develop gravitational wave astronomy.

VI. ACKNOWLEDGMENTS

We would like to thank Peter R. Saulson for his support, advice, and comments; Valerie Williams for careful editing, Andri M. Gretarsson and Steve Penn for careful reading and comments. One of us (GMH) would like to thank the MIT LIGO group for support while finishing the manuscript. The LIGO Visitors Program was instrumental in completing this work; we thank Syd Meshkov, Barry Barish, Gary Sanders, and Rai Weiss for their help. We also thank Rai Weiss for helpful comments on the sources, Kip Thorne for help and inspiration, as well as Gabriela Gonzalez, David Tanner, and Gary Sanders for careful reading and comments. The sources were modeled on computers at the Harvard-Smithsonian Center for Astrophysics and MIT. We especially thank L. Sam Finn for making BENCH available to us as well as everyone who contributed to its development. This work was supported by Syracuse University, U.S. National Science Foundation Grant No. PHY-9900775 and 9603177, the University of Glasgow, and PPARC.

TABLE I. Parameters used in model of spherical, resonant mass, gravitational wave antennas.

| Parameter | Name | Value | Source |
|-----------|--------------------------------------|-------------------------------------|---------|
| Q_s | Sphere quality factor, Al | 40×10^6 | [28] |
| Q_1 | Intermediate mass quality factor, Al | 40×10^6 | [28] |
| Q_2 | Transducer mass quality factor, Nb | 40×10^6 | [29,30] |
| T | Temperature | 50 mK | [26] |
| T_n | SQUID noise number | 1 | [24] |
| d_c | Sensing coil diameter | 9 cm | [2,31] |
| κ | Electrical spring constant per area | 3.78×10^8 N/m ³ | [2] |
| m_s/m_1 | Mass ratio | 100 | [2] |
| m_1/m_2 | Mass ratio | 100 | [2] |

TABLE II. Parameters used for model of interferometric gravitational wave detector.

| Parameter | Name | Value | Source |
|----------------------|--|------------------------------------|------------|
| L | Interferometer arm length | 4000 m | [33] |
| L_{rec} | Recycling cavity length | 10 m | |
| f_{seismic} | Seismic noise cutoff | 10 Hz | [33,50,51] |
| λ | Wavelength of laser light | $1.064 \mu\text{m}$ | [33] |
| P | Laser Power | 125 W | [33,52] |
| η | Photodiode quantum efficiency | 0.9 | [53] |
| w_1 | Gaussian width of laser at input mirror | 6 cm | |
| w_2 | Gaussian width of laser at end mirror | 6 cm | |
| α | Relative power loss in beamsplitter | 3.5×10^{-3} | |
| β | Relative power loss at each mirror | 3.75×10^{-5} | |
| a_{coat} | Relative absorption of coating at input mass | 1×10^{-6} | |
| A_g | Beamsplitter material absorption coefficient | $40 \times 10^{-4} \text{ m}^{-1}$ | |
| t_{BS} | Thickness of beamsplitter | 12 cm | |
| t_1^2 | Power transmittance of input mirror | 0.03 | |
| t_3^2 | Power transmittance of signal recycling mirror | 0.005 | |
| r | Radius of mirrors | 14 cm | |
| ℓ | Thickness of mirrors | 12 cm | |
| ϕ | Mirror material loss angle | 5.0×10^{-9} | [34] |
| L_{sus} | Length of suspension | 0.588 m | |
| d | Total ribbon thickness | 1.7 mm | |
| ϕ_{bulk} | Loss angle for the bulk ribbon material | 3.3×10^{-8} | [43] |
| d_s | Dissipation depth of ribbon material | $182 \mu\text{m}$ | [43] |

 TABLE III. Parameters of the signal recycling mirror to simulate the frequency response of spheres. The transmittance of the input mirrors was held constant at $t_1^2 = 0.03$. The transmittance of the signal recycling mirror was held constant at $t_3^2 = 0.005$. Note that the resonance frequency of the 1.25 m sphere in [2] was a typographical error, the value listed here is correct.

| Diameter d_{sph} (m) | Frequency f_0 (Hz) | Bandwidth $\Delta f/f_0$ | Phase δ |
|-------------------------------|----------------------|--------------------------|----------------|
| 3.25 | 795 | 0.170 | 0.2271 |
| 2.75 | 940 | 0.172 | 0.1921 |
| 2.35 | 1100 | 0.182 | 0.1641 |
| 2.00 | 1292 | 0.200 | 0.1395 |
| 1.70 | 1520 | 0.225 | 0.1182 |
| 1.45 | 1782 | 0.254 | 0.1005 |
| 1.25 | 2067 | 0.290 | 0.08619 |
| 1.05 | 2461 | 0.330 | 0.07179 |

FIG. 1. Schematic drawing of a spherical, resonant mass, gravitational wave detector with a three-mode transducer attached. The sphere mass, m_s , is connected to mechanical ground, here the center of mass of the sphere. The gravitational wave acts as a force, F , between the sphere mass and ground. Each of the complex spring constants, k_s , k_1 , and k_2 , includes dissipation which gives rise to thermal noise. The transducer mass is next to a superconducting pick up coil which stores a persistent current. This current is shunted to the input coil of the SQUID in proportion to the motion of the mass. The SQUID amplifies the signal and also serves as a source of wideband noise.

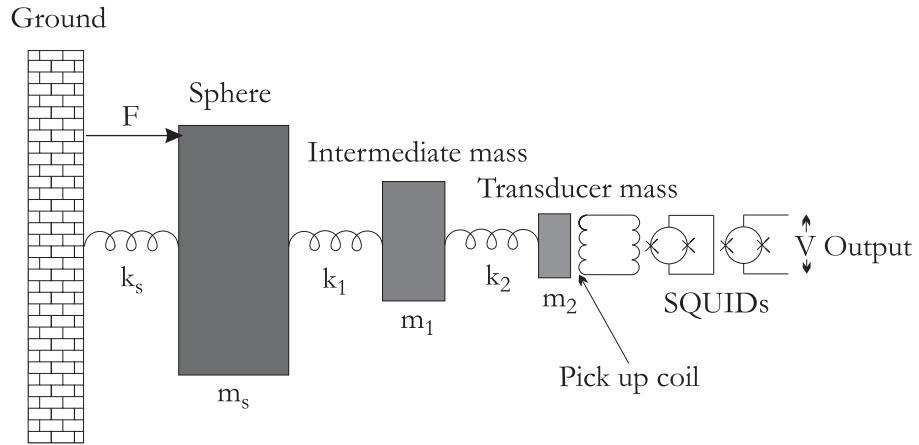


FIG. 2. Strain spectra for a 3.25 m diameter spherical, resonant mass antenna including the components of the noise. The dashed line shows the thermal noise at 50 mK, the dotted line shows the velocity (forward action) amplifier noise from the quantum limited SQUID, and the dashed-dotted line shows the force (back-action) amplifier noise from the same SQUID. The solid line is the total noise from the spherical antenna.

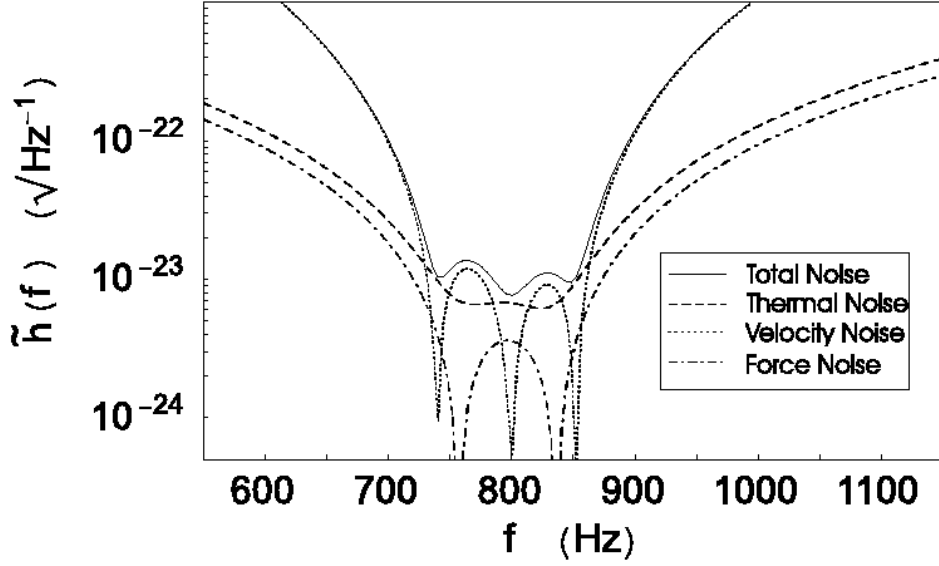
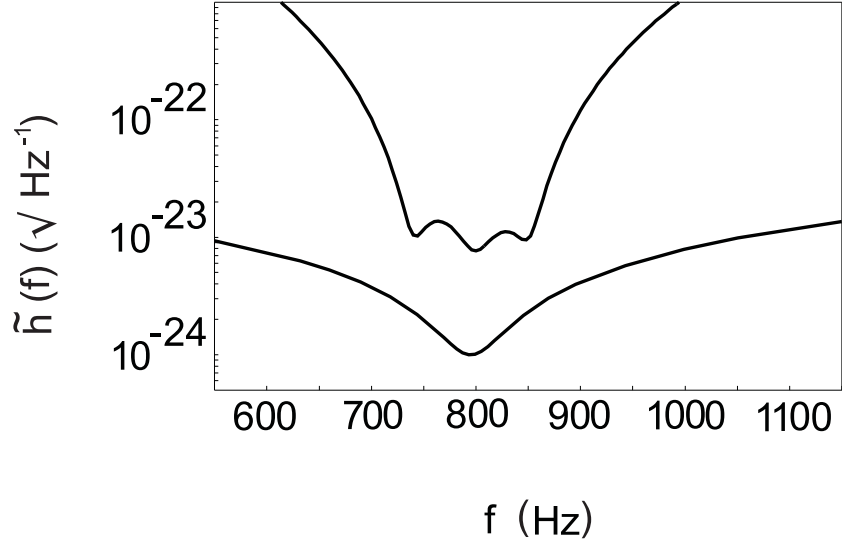


FIG. 3. Strain spectra for narrowband interferometers and spherical, resonant mass antennas.

(A) Both interferometer and sphere are maximally sensitive at 795 Hz, corresponding to the quadrupole mode of an aluminum sphere with diameter 3.25 m and a phase shift $\delta = 0.2271$ for the interferometer.

(B) Strain spectra for four narrowband interferometers, sensitive at 795 Hz, 1100 Hz, 1520 Hz, and 2067 Hz. Also shown are the strain spectra for the four spherical, resonant mass antennas with the same resonance frequencies. The spheres are less sensitive than the interferometers at the resonance point, but have roughly the same sensitivity as the interferometers off-resonance.

(A)



(B)

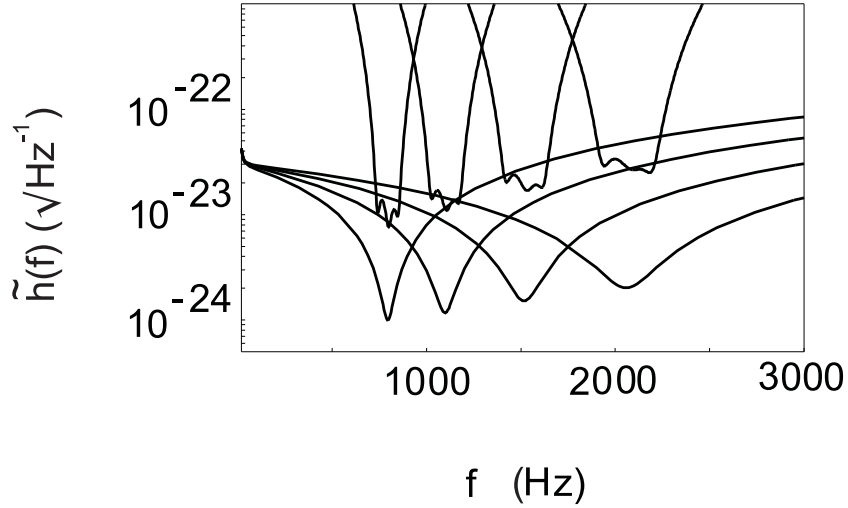


FIG. 4. Schematic drawing of an interferometric gravitational wave detector equipped for resonant sideband extraction. The laser creates a light beam which is sent through the power recycling mirror into two arms of a Michelson interferometer. The signal exits at the output port through the signal recycling mirror, which forms an additional Fabry-Perot cavity with the Michelson interferometer. Finally, the signal is detected past the signal recycling mirror with a photodiode.

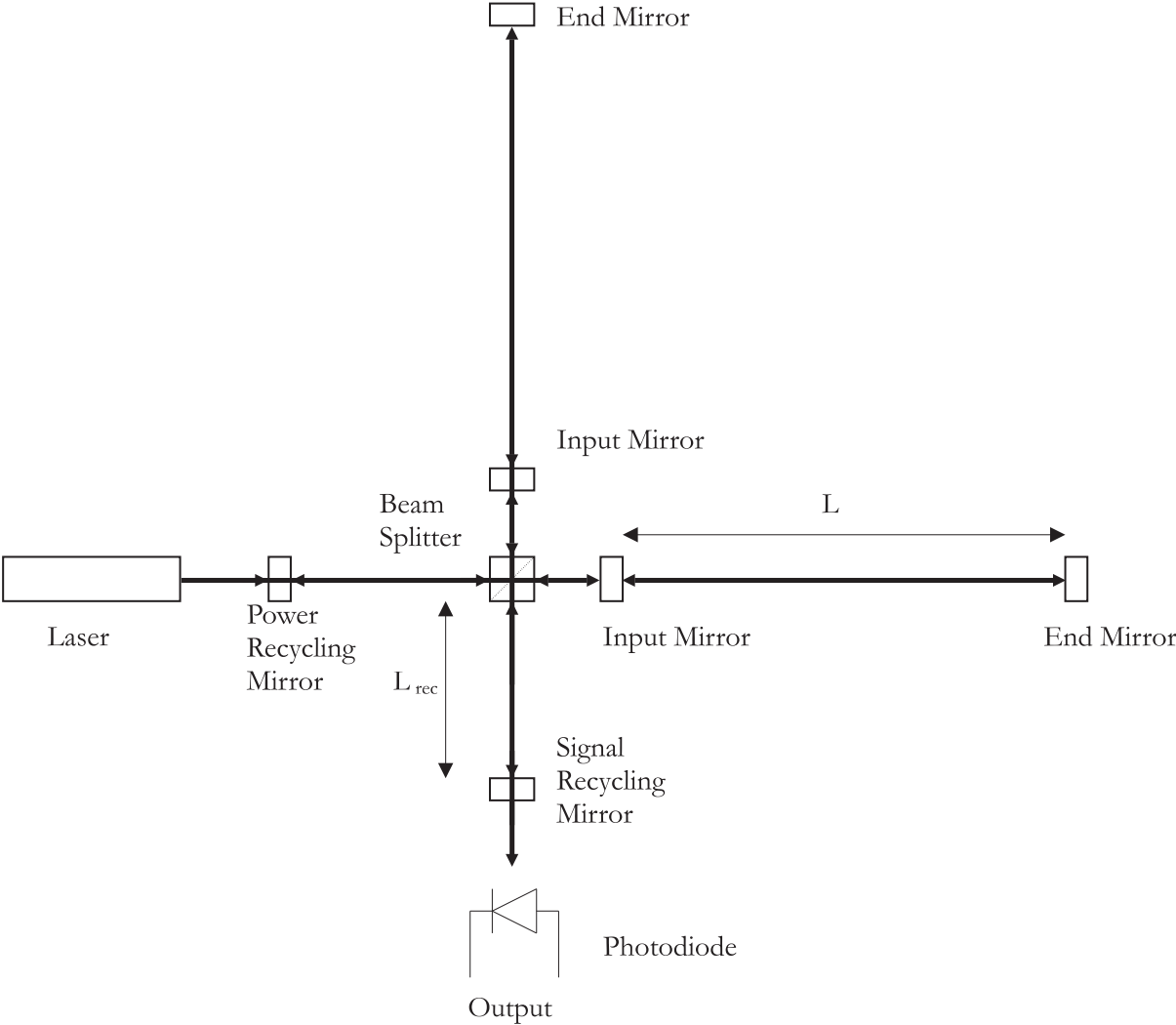
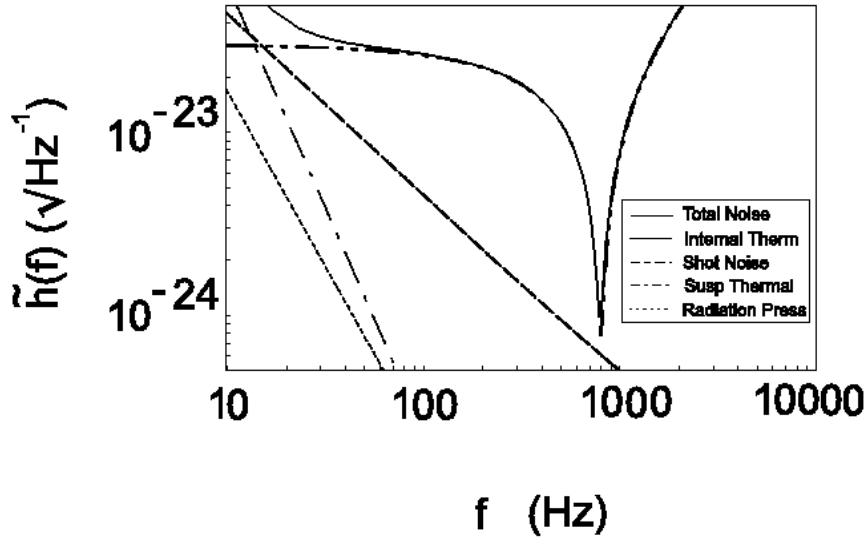


FIG. 5. Strain spectra for an interferometric gravitational wave detector with resonant sideband extraction showing all the components of the noise. The dash-dotted-dotted line shows the shot noise from a 125 W laser, the dashed line shows the sapphire mirrors' internal mode thermal noise, and the dashed-dotted line shows the thermal noise from the ribbon suspension, and the dotted line shows the radiation pressure. The solid line is the total noise.

(A) The noise components when the interferometer is in a narrowband configuration tuned to 795 Hz.

(B) The noise components when the interferometer is in a broadband configuration optimized for binary neutron star inspiral.

(A)



(B)

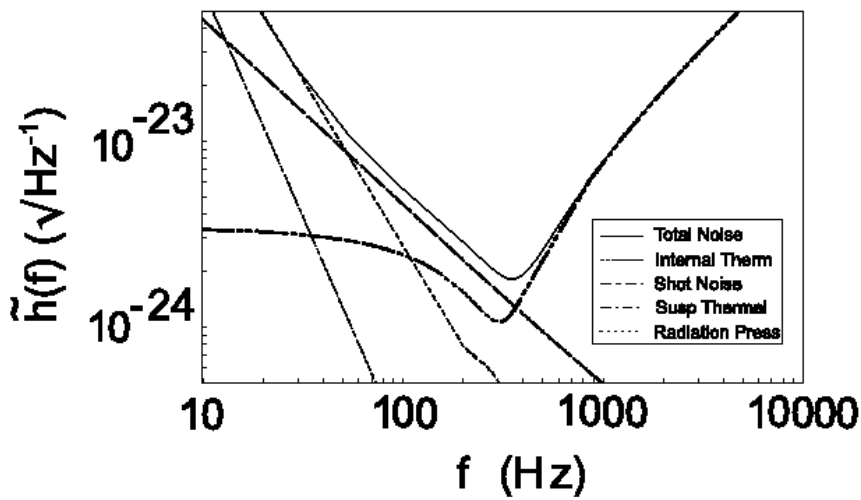
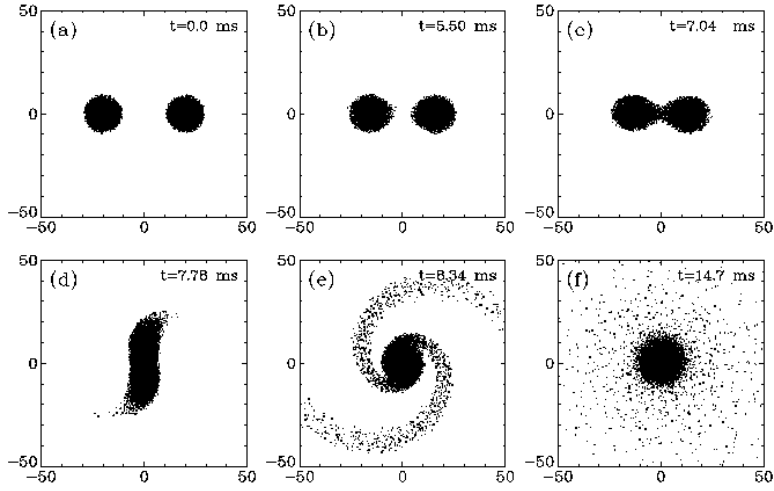


FIG. 6. Inspiring and coalescing binary neutron stars.

(A) Particle positions for each neutron star during the coalescence phase. The stars first fall together, reducing the gravitational wave amplitude at twice the instantaneous orbital velocity. Then a bar forms which creates an increased amplitude at twice the rotational velocity.

(B) The frequency domain gravitational waveform averaged over source orientation. Notice the slight dip just above 1000 Hz from the in-fall and the peak near 3500 Hz from the bar. Each neutron star was modeled as having a mass of $1.4 M_{\odot}$, an equatorial radius of 10 km, and a distance from the antenna of 15 Mpc.

(A)



(B)

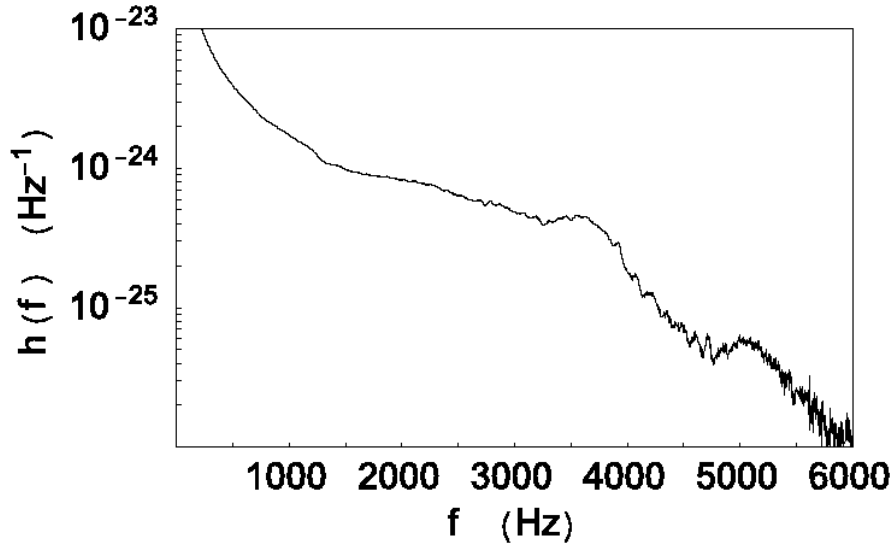
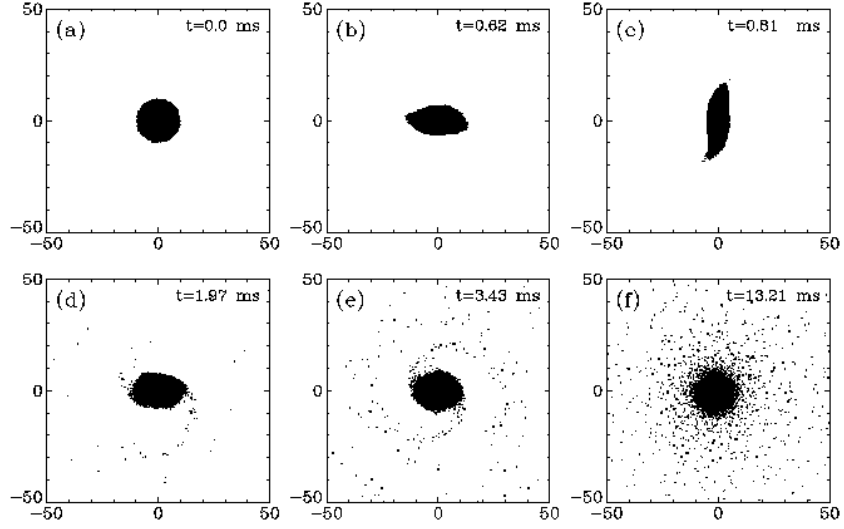


FIG. 7. A rapidly rotating stellar core undergoing a dynamical instability.
 (A) Particle positions for the neutron star during the gravitational wave emission which shows the bar shape that develops from the instability.
 (B) The frequency domain gravitational waveform averaged over source orientation. The star was modeled as having a mass of $1.4 M_{\odot}$, an equatorial radius of 10 km, and a distance from the antenna of 1 Mpc.



(B)

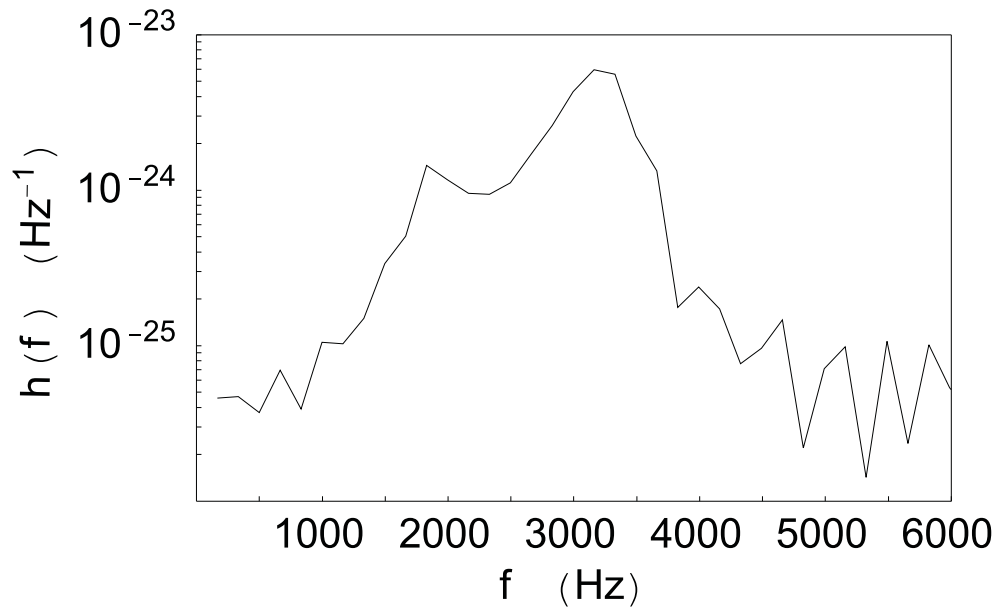
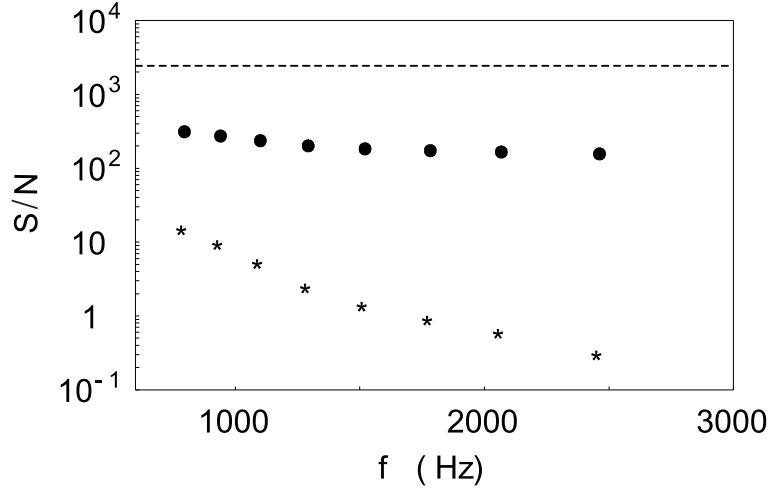


FIG. 8. Energy signal-to-noise ratios for binary neutron star inspiral and coalescence. This source was simulated interacting with spherical resonant mass antennas (shown with asterisks) and interferometers operating with resonant sideband extraction (shown with circles) and a broadband interferometer (shown with a dotted line).

(A) The binary neutron stars were assumed at a distance of 15 Mpc. This distance is the closest estimated for a single event a year. Both detectors have high enough SNR's to reach this distance.

(B) The binary neutron stars were assumed at a distance of 200 Mpc. This distance is enough for multiple events for year, and advanced LIGO with RSE does have a SNR high enough to reach this distance.

(A)



(B)

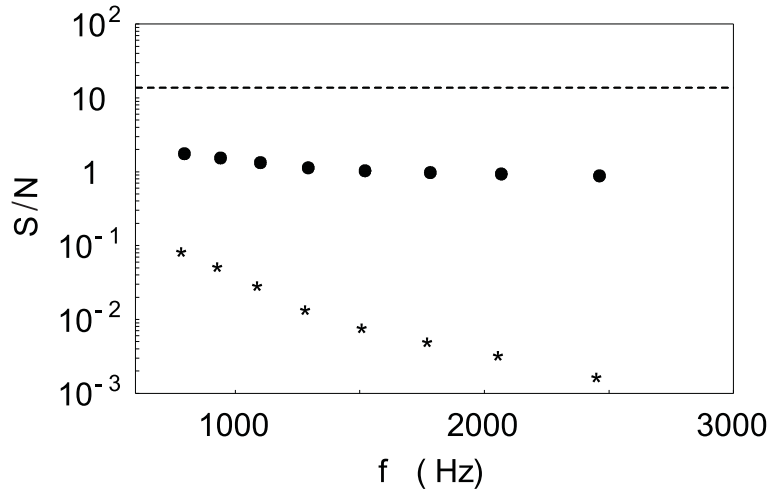
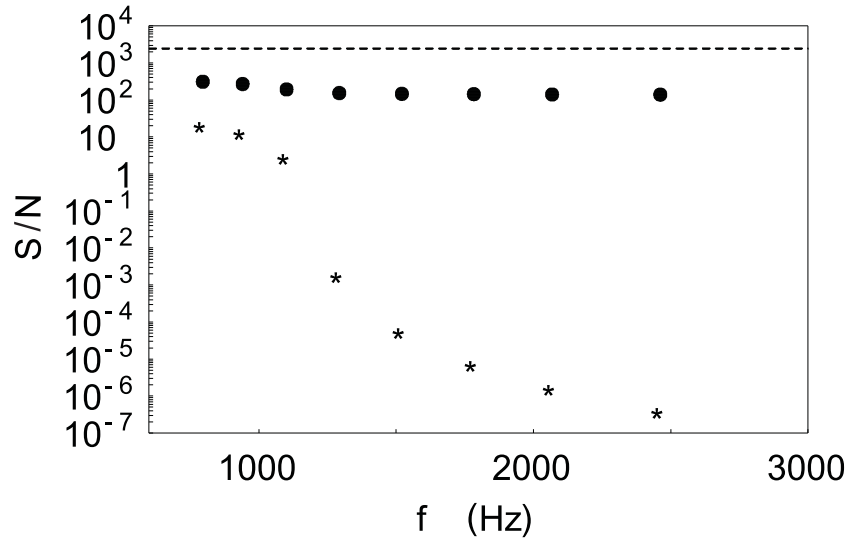


FIG. 9. Energy signal-to-noise ratios for binary neutron star separated into an inspiral and coalescence phase at 15 Mpc. The waveform was divided at the dynamical instability frequency, when the neutron stars are about 20 km apart. This source was simulated interacting with spherical resonant mass antennas (shown with asterisks) and interferometers operating with resonant sideband extraction (shown with circles) and a broadband interferometer (shown with a dotted line).

(A) The binary neutron star inspiral phase.

(B) The binary neutron star coalescence phase.



(B)

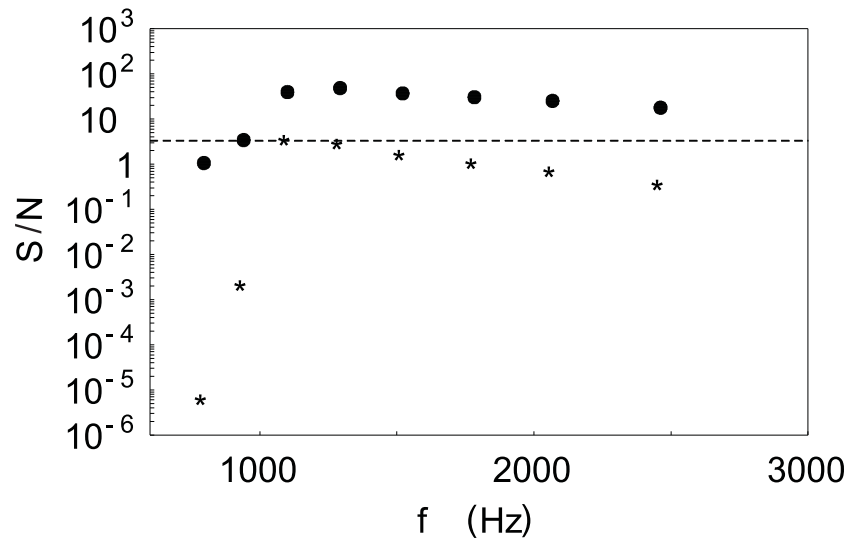
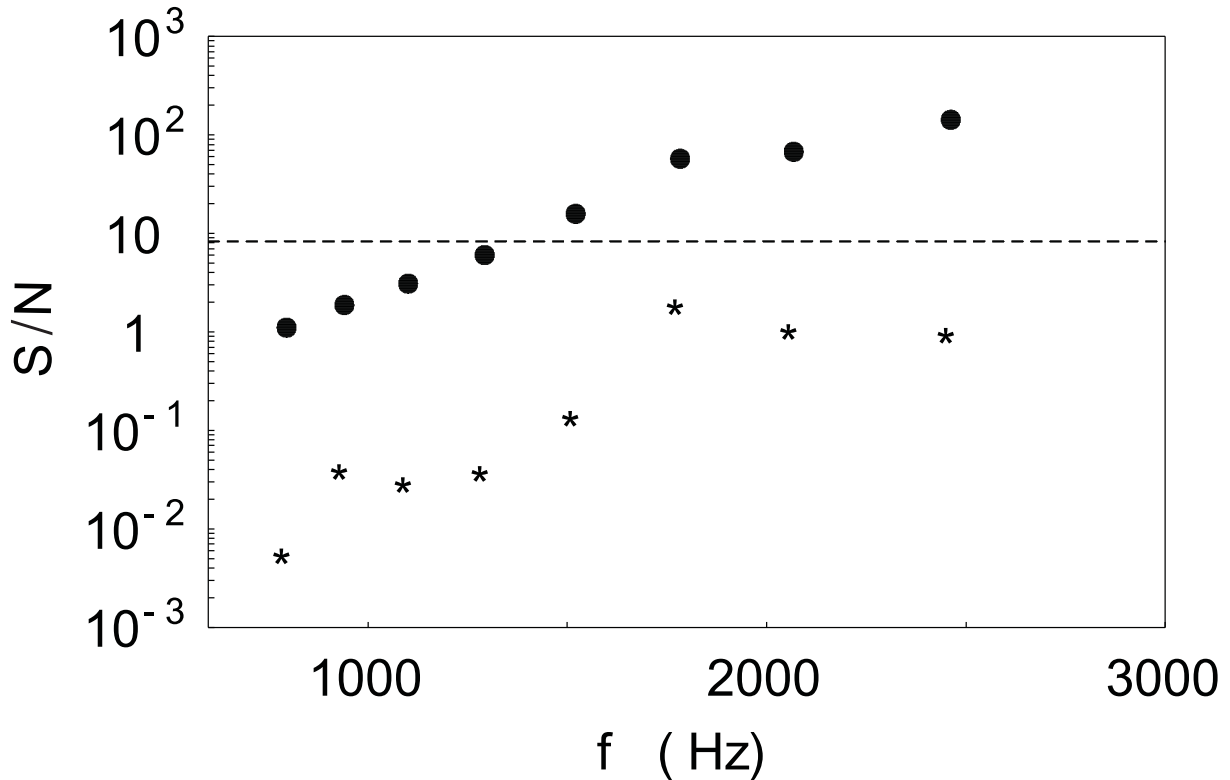


FIG. 10. Energy signal-to-noise ratios for a rapidly rotating stellar core undergoing a dynamical instability. This source was simulated interacting with spherical resonant mass antennas (shown with asterisks) and interferometers operating with resonant sideband extraction (shown with circles). The rapidly rotating core event was assumed at a distance of 1 Mpc.



-
- [1] J. Weber, Phys. Rev. **117**, 306 (1960).
[2] G. M. Harry, T. R. Stevenson, and H. J. Paik, Phys. Rev. D **54**, 2409 (1996).
[3] S. M. Merkowitz and W. W. Johnson, Phys. Rev. D **51**, 2546 (1995).
[4] A. Abramovici *et al*, Science, **256** 325, 1992.
[5] B. J. Meers, Phys. Rev. D **38**, 2317, 1988.
[6] J. Mizuno, K. A. Strain, P. G. Nelson, J. M. Chen, R. Schilling, A. Rüdiger, W. Winkler, and K. Danzmann, Phys. Lett. A **175**, 273, 1993.
[7] J. L. Houser, in preparation.
[8] J. L. Houser, proceedings of the Third Edoardo Amaldi Conference on Gravitational Waves, July 12-16, 1999 California Institute of Technology, American Institute of Physics.
[9] K. Thorne, in *Proceedings of the Snowmass 95 Summer Study on Particle and Nuclear Astrophysics and Cosmology*, 1995, eds. E. W. Kolb and R. Peccei, World Scientific, Singapore; also published in *Particle Physics, Astrophysics and Cosmology*, Proceedings of the SLAC Summer Institute on Particle Physics, eds. Jennifer Chan and Lilian DePorcel (SLAC-Report-484, Stanford Linear Accelerator Center, Stanford, CA, 1996).
[10] E. S. Phinney, Astrophys. J., **380**, L17.
[11] V. Kalogera, R. Narayan, D. N. Spergel, J. H. Taylor, Astrophys. J., to be published, astro-ph/0012038.
[12] V. Kalogera, Astrophys. J. **541**, 319, (2000).
[13] K. Thorne, *300 Years of Gravitation*, ed. S.W. Hawking and W. Israel, (New York: Cambridge University Press).
[14] J. C. N. de Araujo, O. D. Miranda, O. D. Aguiar, Phys. Rev. D **61**, 124015 (2000).
[15] J. C. Price, Phys. Rev. D **36**, 3555 (1987).
[16] T. R. Stevenson, in *Gravitational Wave Experiments*, proceedings of the First Edoardo Amaldi Conference, Frascati, Italy, edited by E. Coccia, G. Pizzella and F. Ronga (World Scientific, Singapore, 1995).

- [17] E. Coccia, V. Fafone, G. Frossati, J. A. Lobo, J. A. Ortega, Phys. Rev. D **57**, 2051, (1998).
- [18] W. W. Johnson *et al.*, in *Gravitational Wave Experiments*, proceedings of the First Edoardo Amaldi Conference, Frascati, Italy, edited by E. Coccia, G. Pizzella and F. Ronga (World Scientific, Singapore, 1995).
- [19] J. P. Zendri, L. Baggio, M. Bonaldi, M. Cerdonio, L. Conti, V. Crivelli Visconti, P. Falferi, P. L. Fortini, V. Martinucci, R. Mezzena, A. Ortolan, G. A. Prodi, G. Soranzo, L. Taffarello, G. Vedovato, A. Viante, S. Vitale, proceedings of the Third Edoardo Amaldi Conference on Gravitational Waves, July 12-16, 1999 California Institute of Technology, American Institute of Physics.
- [20] M. McHugh (private communication).
- [21] W. M. Folkner, Ph. D. thesis, University of Maryland, 1987.
- [22] D. D. Awschalom *et al.*, Phys. Rev. Lett. **62**, 199 (1989); M. W. Cromar and P. Carelli, Appl. Phys. Lett. **38**, 723 (1981); D. J. Van Harlingen, R. H. Koch, and J. Clarke, Physica (Utrecht) **108B**, 1083 (1981).
- [23] I. Jin, A. Amar, and F. C. Wellstood, Appl. Phys. Lett. **70**, 2186 (1997).
- [24] G. M. Harry, I. Jin, T. R. Stevenson, H. J. Paik, F. C. Wellstood, Appl. Phys. Lett. **76**, 1446 (2000).
- [25] C. Z. Zhou and P. F. Michelson, Phys. Rev. D **51**, 2517 (1995).
- [26] E. Coccia *et al.*, in *Gravitational Wave Experiments, Proceedings of the First Edoardo Amaldi Conference*, Frascati, Italy, edited by E. Coccia, G. Pizzella, and F. Ronga (World Scientific, Singapore, 1995).
- [27] P. Astone, M. Bassan, P. Bonifaze, P. Carelli, E. Coccia, C. Cosmelli, V. Fafone, S. Frasca, A. Marini, G. Mazzitelli, Y. Minenkov, I. Modena, G. Modestino, A. Moleti, G. V. Pallottino, M. A. Papa, G. Pizzella, P. Rapagnani, F. Ricci, F. Ronga, R. Terenzi, M. Visco, L. Votano, *Astropart. Phys.* **7**, 231 (1997).
- [28] W. Duffy, J. Appl. Phys. **68**, 5601 (1990)
- [29] W. Duffy and R. Umstattd, J. App. Phys. **75** 4489 (1994).
- [30] Z. Geng, Ph. D. thesis, Louisiana State University, 1994.
- [31] G. Harry, Ph. D. thesis, University of Maryland College Park, 1999.
- [32] The program BENCH is available at <http://fiji.nirvana.phys.psu.edu/~lsf/Benchmarks/>
- [33] *LSC White Paper on Detector Research and Development*. Available at <http://www.ligo.caltech.edu/docs/T/T990080-00.pdf>
- [34] V. B. Braginsky, V. P. Mitrofanov, and V. I. Panov, *Systems with small dissipation* (The University of Chicago Press, Chicago, 1985).
- [35] S. Rowan, G. Cagnoli, P. Sneddon, J. Hough, R. Route, E. K. Gustafson, M. M. Fejer, V. Mitrofanov, Phys. Lett. A. **265**, 5 (2000).
- [36] V. B. Braginsky, M. L. Godoretsky, and S. P. Vyatchanin, Phys. Lett. A **264**, 1 (1999).
- [37] F. Bondu, P. Hello, J. V. Vinet, Phys. Lett. A **246**, 227 (1998).
- [38] Y. T. Liu and K. S. Thorne, Phys. Rev. D. **62**, 122002 (2000).
- [39] A. M. Gretarsson, G. M. Harry, S. D. Penn, P. R. Saulson, J. J. Schiller, and W. J. Startin, in proceedings of the Third Edoardo Amaldi Conference on Gravitational Waves, edited by S. Meshkov (American Institute of Physics, Melville, New York, 2000) physics/9911040.
- [40] S. Rowan, oral presentation, 2001 Aspen Winter Conference on Gravitational Waves, (Aspen, Colorado, USA, 2001); A. Gretarsson, oral presentation, 2001 Aspen Winter Conference on Gravitational Waves, (Aspen, Colorado, USA, 2001), http://www.ligo.caltech.edu/%7Everonica/Aspen2001/pdf/gretarsson_new.pdf.
- [41] S. D. Penn, G. M. Harry, A. M. Gretarsson, S. E. Kittelberger, P. R. Saulson, J. J. Schiller, J. R. Smith, and S. O. Swords, submitted to Rev. Sci. Instrum. gr-qc/0009035.
- [42] J. Kovalik and P. R. Saulson, Rev. Sci. Instrum. **64**, 2942 (1993).
- [43] A. M. Gretarsson and G. M. Harry, Rev. Sci. Instrum. **70**, 4081 (1999).
- [44] W. J. Startin, M. A. Beilby, and P. R. Saulson, Rev. Sci. Instrum. **69**, 3681 (1998).
- [45] A. M. Gretarsson, G. M. Harry, P. R. Saulson, S. D. Penn, W. J. Startin, J. Hough, S. Rowan, G. Cagnoli, Phys. Lett. A, in press. gr-qc/9912057.
- [46] C. Zener, Phys. Rev. **52** 230 (1937).
- [47] S. Rowan, R. Hutchins, A. McLaren, N. A. Robertson, S. M. Twyford, and J. Hough, Phys. Lett. A, **227** 153 (1997).
- [48] A. Buonanno and Y. Chen, gr-qc/0010011, gr-qc/0102012.
- [49] K. A. Strain, K. Danzmann, J. Mizuno, P. G. Nelson, A. Rüdiger, R. Schilling, W. Winkler, Phys. Lett. A, **194** 124 (1994).
- [50] J. Giame, B. Lantz, D. DeBra, J. How, C. Hardham, S. Richman, and R. Stebbins, proceedings of the Third Edoardo Amaldi Conference on Gravitational Waves, July 12-16, 1999 California Institute of Technology, American Institute of Physics.
- [51] A. Bertolini, G. Cella, E. D'Ambrosio, R. DeSalvo, V. Sannibale, A. Takamori, H. Yamamoto, in proceedings of the Third Edoardo Amaldi Conference on Gravitational Waves, edited by S. Meshkov (American Institute of Physics, Melville, New York, 2000).
- [52] T. S. Rutherford, W. M. Tulloch, E. K. Gustafson and R. L. Byer, IEEE Journal of Quantum Electronics, **36**, 205 (2000).
- [53] D. Jackerl (private communication).
- [54] L. Hernquist and N. Katz, Astron. Journal, Supplement Series, **70**, 419 (1989).
- [55] R. Narayan, T. Piran, and A. Shemi, Astrophys. J., **379**, L17.

- [56] L. S. Finn and D. Chernoff, *Phys. Rev. D*, **47**, 2198.
- [57] C. Cutler, T. A. Apostolatos, L. Bildsten, L. S. Finn, E. E. Flanagan, D. Kennefick, D. M. Markovic, A. Ori, E. Poisson, G. J. Sussman, and K. S. Thorne, *Phys. Rev. Lett.*, **70**, 2984.
- [58] C. Cutler and E. Flanagan, *Phys. Rev. D*, **49**, 2658.
- [59] K. Thorne, in *Compact Stars in Binaries*, Proceedings of IAU Symposium 165, edited by J. van Paradijs, E. van den Heuvel, and E. Kuulkers (Kluwer, Dordrecht).
- [60] V. Kalogera, in proceedings of the Third Edoardo Amaldi Conference on Gravitational Waves, edited by S. Meshkov (American Institute of Physics, Melville, New York, 2000).
- [61] B. F. Schutz, *Relativistic Gravitational Experiments in Space*, ed. M. Demianski and G.W.G. Everitt (Singapore: World Scientific).
- [62] X. Zhuge, J. M. Centrella, and S. L. W. McMillan, *Phys. Rev. D*, **50**, 6247.
- [63] X. Zhuge, J. M. Centrella, and S. L. W. McMillan, *Phys. Rev. D*, **54**, 7261.
- [64] C. Misner, K. Thorne, and J. Wheeler, *Gravitation* (Freeman, New York).
- [65] S. Bonazzola and E. Gourgoulhon, *Astron. Astrophys.*, **312**, 675.
- [66] P. J. Armitage and C. J. Clarke, *Mon. Not. Roy. Astron. Soc.*, **280**, 458.
- [67] J. L. Houser, work in progress.
- [68] S. L. Detweiler and L. Lindblom *Astrophys. J.*, **213**, 193.
- [69] B. F. Schutz, *Dynamical Spacetimes and Numerical Relativity*, ed. J. Centrella (New York: Cambridge University Press).
- [70] D. Lai and S. L. Shapiro, *Astrophys. J.*, **442**, 259.
- [71] S. Smith, J. Houser, and J. Centrella, *Astrophys. J.*, **458**, 236.
- [72] J. L. Houser and J. M. Centrella, *Phys. Rev. D*, **54**, 7278.
- [73] J. L. Houser, *Mon. Not. R. Astron. Soc.* **299**, 1069 (1998).
- [74] C. L. Fryer and A. Heger, *Astrophys. J.* **541**, 1033 (2000), astro-ph/9907433.
- [75] M. Maggiore, *Phys. Rept.* **331**, 283 (2000).
- [76] S. Vitale, M. Cerdonio, E. Coccia and A. Ortolan, *Phys. Rev. D* **55**, 1741 (1997).
- [77] E. Coccia, F. Fucito, J. A. Lobo, M. Salvino, *Phys. Rev. D*, **62**, 044019 (2000).
- [78] J. A. Faber, F. A. Rasio, J. B. Manor, *Phys. Rev. D* **63**, 044012 (2001).
- [79] M. Maggiore and A. Nicolis, *Phys. Rev. D* **62**, 02004 (2000).
- [80] M. Bianchi, M. Brunetti, E. Coccia, F. Fucito and J. A. Lobo, *Phys. Rev. D* **57**, 4525 (1998).